Research Square

Preprints are preliminary reports that have not undergone peer review.
They should not be considered conclusive, used to inform clinical practice,
or referenced by the media as validated information.

Topology-dependent surface diffusion and structural relaxation in silicon membrane– cavity formation

Jungchul Lee

jungchullee@kaist.ac.kr

Korea Advanced Institute of Science and Technology

Research Article

Keywords:

Posted Date: November 20th, 2026

DOI: https://doi.org/10.21203/rs.3.rs-11679562/v1

License: This work is licensed under a Creative Commons Attribution 4.0 International License.
Read Full License

Additional Declarations: No competing interests reported.

Topology-dependent surface diffusion and structural relaxation in silicon membrane–cavity formation

Jungchul Lee*

Department of Mechanical Engineering, Korea Advanced Institute of Science and Technology

*Corresponding author: Jungchul Lee. E-mail(s):jungchullee@kaist.ac.kr

Abstract

Surface-diffusion-driven morphological evolution is commonly described in terms of local geometric factors such as curvature, feature size, and diffusion distance, whereas the role of interface topology in long-range surface mass transport remains less understood. Here, we investigate topology-dependent buried cavity formation in periodic hole lattices using three-dimensional phase-field simulations combined with graph-based transport analysis. Square, triangular, and honeycomb lattices exhibit markedly different sealing kinetics and post-sealing structural relaxation despite identical material properties, feature dimensions, and annealing conditions, demonstrating that local geometric descriptors alone are insufficient to characterize their evolution. To quantify this topology dependence, we introduce transport accessibility as a topology-resolved descriptor of the interconnected pathways available for surface mass redistribution. By representing the evolving Si/void interface as a transport network and combining geodesic transport distance with equivalent network conductance, we formulate a conductance-corrected transport resistance that improves the quantitative description of characteristic relaxation kinetics across the investigated lattice geometries. Analysis of the evolving surface-transport field independently supports the network-based interpretation and reveals that post-sealing relaxation is jointly regulated by transport-path length and pathway accessibility. These findings demonstrate that interface connectivity, together with transport-path length, plays an important role in the surface-diffusion-driven relaxation of silicon membrane–cavity structures. The proposed transport analysis provides a physically motivated approach for interpreting topology-dependent morphological evolution and offers useful guidance for the design of diffusion-formed semiconductor architectures.

1. Introduction

Surface-diffusion-driven morphological evolution plays a central role in the formation and transformation of semiconductor micro- and nanostructures [1,2]. During high-temperature annealing, capillarity-driven surface diffusion redistributes material along evolving interfaces, enabling substantial changes in morphology and topology without material addition or removal [1,3]. Related morphological transformations, including solid-state dewetting of thin films, have also been extensively investigated [4]. Understanding this evolution is important not only for describing the underlying kinetics of diffusion-controlled interface relaxation but also for controlling the resulting three-dimensional architectures. In semiconductor systems, such self-organized evolution has been exploited to form buried cavities and suspended membranes, providing scalable fabrication routes for silicon-on-nothing (SON) structures and their applications in MEMS pressure sensors, resonant vacuum sensors, photonic pressure sensors, and other monolithically integrated cavity-based microsystems [3,5–12]. Because the resulting morphology directly determines the mechanical, optical, and thermal characteristics of these structures, establishing a quantitative understanding of surface-diffusion-driven evolution is essential for both fundamental control of interface morphology and rational design of diffusion-formed semiconductor architectures.

Previous studies have primarily focused on how local geometric parameters—including hole diameter, hole pitch, membrane thickness, and annealing conditions—affect surface-diffusion kinetics, sealing behavior, and the resulting buried cavity morphology [13–15]. These studies established that morphological evolution is governed by curvature-induced capillary forces and surface diffusion, consistent with the classical theories [1,2,16]. Consequently, diffusion-driven structural evolution has generally been interpreted using local geometric descriptors, including surface curvature, characteristic diffusion distance, feature dimensions, and surface-diffusion kinetics. Although these descriptors successfully describe the local thermodynamic driving force and transport kinetics, they do not explicitly account for how the global connectivity of the evolving interface influences long-range surface mass redistribution. Consequently, an equally fundamental structural parameter has received far less attention: the topology of the hole lattice. Even when the initial hole diameter, depth, and pitch are identical, changes in lattice connectivity alter both the number of neighboring holes participating in material redistribution and the accessibility of interconnected diffusion pathways available for long-range surface transport. These considerations suggest that lattice topology influences not only sealing kinetics but also post-sealing structural relaxation by regulating transport accessibility in addition to conventional geometric factors such as curvature and diffusion distance.

Despite this physical significance, a systematic investigation of topology-dependent morphological evolution remains lacking. Experimental comparison of different lattice topologies is complicated by process variability and by the difficulty of continuously observing evolving three-dimensional morphologies during high-temperature annealing. Computational modeling therefore provides a powerful approach for isolating the intrinsic influence of lattice topology under rigorously controlled conditions. Phase-field simulation is particularly well suited because it naturally captures curvature-driven surface diffusion while preserving complex interface evolution throughout the sealing process [17–19], and has been successfully applied to membrane–cavity formation and morphology evolution in silicon- and germanium-on-nothing structures [20,21]. However, conventional phase-field analyses primarily describe temporal morphological evolution and do not directly quantify how evolving interface

topology influences long-range transport pathways. To overcome this limitation, the simulated interfaces are further analyzed using graph-based transport analysis, enabling direct evaluation of topology-dependent transport accessibility under identical material properties, geometric dimensions, and annealing conditions. This combined computational framework enables comparison of lattice arrangements under matched feature dimensions, material properties, and processing conditions, while acknowledging differences in initial void-area fraction.

Here, we investigate topology-dependent buried cavity formation in three representative periodic hole lattices—square, triangular, and honeycomb—using three-dimensional phase-field simulations under identical geometric and processing conditions. To quantify the influence of interface topology on long-range surface transport, we introduce transport accessibility as a topology-resolved descriptor characterizing the accessibility of interconnected diffusion pathways during structural evolution. By combining geodesic transport pathways with equivalent resistor-network conductance, we establish a conductance-corrected transport resistance that relates interface topology to post-sealing structural relaxation. Direct analysis of the evolving surface-transport field further clarifies the relationship between interface connectivity and surface mass redistribution. Together, these results provide a quantitative perspective on topology-dependent structural relaxation and its implications for controlling buried cavity formation in silicon-based microstructures.

2. Numerical configuration

Three representative periodic hole lattices—square, triangular, and honeycomb—were constructed to investigate the influence of lattice topology on surface-diffusion-driven morphological evolution (Fig. 1). All lattices employed an identical cylindrical hole diameter of 100 nm, a nearest-neighbor center-to-center spacing (pitch) of 150 nm, a hole depth of 400 nm, and a silicon film thickness of 800 nm. An initial 200-nm-thick void layer was placed above the silicon surface to provide sufficient space for surface evolution during annealing. The lattices differed in their spatial arrangement and nearest-neighbor coordination numbers (z_c = 4, 6, and 3 for the square, triangular, and honeycomb lattices, respectively). Their initial planar void-area fractions were approximately 34.9%, 40.3%, and 26.9%, respectively, for the specified hole diameter and nearest-neighbor spacing. Thus, lattice arrangement also changes the initial void volume per unit planar area, and its influence cannot be separated completely from connectivity in the present comparison. Here, “topology” refers to the organization of the initial hole lattice and, during evolution, to connectivity changes of the enclosed void regions; the term is not intended to imply that coordination number is the only differing geometric property.

Figures 1a–c illustrate the computational domains used for the three lattice geometries. The square and triangular lattices were represented by a single periodic unit cell because of their mirror symmetry (Figs. 1a,b), whereas the honeycomb lattice required a larger periodic supercell containing multiple inequivalent hole positions (Fig. 1c). The corresponding cross sections used for quantitative analyses are shown in Figs. 1d and 1e. Specifically, the A–A′ section was used for the square and triangular lattices (Fig. 1d), whereas the B–B′ section was used for the honeycomb lattice (Fig. 1e) to quantify membrane and cavity evolution.

Periodic boundary conditions were imposed in both lateral directions to represent an infinite periodic array, whereas a zero-normal-flux boundary condition was applied at the bottom substrate surface. The upper surface was treated as a free surface undergoing curvature-driven

surface diffusion. All simulations were performed using identical material properties, numerical parameters, and annealing conditions.

To quantify topology-dependent surface transport, the evolving phase-field morphology was converted into a weighted interfacial graph (Fig. S1). The Si/void interface was extracted from the $\phi = 0.5$ isosurface, and diffuse-interface voxels satisfying $0.1 \leq \phi \leq 0.9$ were defined as graph nodes. Adjacent nodes were connected using six-neighbor connectivity with edge weights equal to the corresponding voxel-center distances. Interface-constrained shortest paths and geodesic-distance fields were subsequently computed using a multi-source Dijkstra algorithm [22], from which the transport-accessibility descriptor was evaluated.

The phase-field equation was discretized on a uniform Cartesian grid using second-order central finite differences and integrated using an explicit forward Euler scheme with adaptive time stepping. The dimensionless simulation time was defined as $t^* = \sum_i \Delta t_i$, where Δt_i denotes the adaptive time increment at the i-th iteration. Based on the temporal and spatial convergence analyses presented in Figs. S2 and S3, all simulations employed a grid spacing of $\Delta x = 5$ nm and a maximum time increment of $\Delta t_{\max} = 5$, ensuring numerically converged solutions while maintaining computational efficiency.

3. Results and Discussion

3.1 Topology-dependent morphological evolution

For each lattice geometry, the phase-field simulation was continued until no further measurable changes in membrane thickness or cavity height were observed, indicating that the post-sealing morphology had reached a quasi-steady state.

Figure 2 compares the morphology evolution of the three lattice geometries under identical initial hole diameter, nearest-neighbor spacing, film thickness, material properties, and annealing conditions. Despite these identical conditions, the square, triangular, and honeycomb lattices exhibit markedly different evolution pathways, showing that differences in lattice arrangement, associated void fraction, and evolving connectivity influence surface-diffusion-driven structural evolution.

All three lattices undergo the same sequence of surface rounding, neck formation, surface sealing, and buried cavity formation. However, the subsequent evolution diverges significantly after surface closure. The square lattice develops an isolated buried cavity that gradually relaxes toward a relatively uniform membrane–cavity structure. The triangular lattice follows a similar evolution but exhibits more rapid lateral neck growth because each hole is connected to six nearest neighbors, resulting in earlier surface sealing and faster structural relaxation. In contrast, the honeycomb lattice forms a laterally connected cavity through merging of adjacent voids across the narrow ligaments separating neighboring holes. This interconnected cavity exhibits a characteristic dumbbell-shaped cross section and evolves substantially more slowly during the post-sealing stage.

These differences indicate that lattice topology influences not only the sealing kinetics but also the transport length scales over which material redistribution occurs during structural relaxation. Whereas the square and triangular lattices primarily undergo localized relaxation beneath individual holes, the interconnected cavity in the honeycomb lattice requires coordinated mass

redistribution over multiple neighboring unit cells. Consequently, topology influences both the final cavity morphology and the characteristic time required to approach the quasi-steady state.

The topology-dependent structural evolution observed in Fig. 2 is quantified in the following sections through measurements of membrane thickness, cavity height, transport accessibility, and characteristic structural relaxation time.

3.2 Topology evolution during cavity formation

Although all three lattice geometries ultimately evolve into membrane–cavity structures, the connectivity of the evolving void network changes through discrete topological transitions during surface-diffusion-driven evolution. To identify surface sealing, the three-dimensional void phase was analyzed using connected-component labeling under periodic lateral boundary conditions [23]. Surface sealing was defined as the loss of connectivity between the exterior void and the retained internal cavity. Separately, the number of enclosed cavity lobes was evaluated in the representative XZ cross section to characterize subsequent morphological transitions associated with cavity merging.

Figure 3a compares the evolution of the normalized minimum surface-opening diameter, $d_{\mathrm{open}}/d_{\mathrm{open},0}$, as a function of dimensionless time. In all three lattices, the opening diameter decreases monotonically as capillarity-driven surface diffusion progressively closes the surface neck. The square and triangular lattices exhibit nearly identical sealing trajectories, whereas the honeycomb lattice evolves more gradually because material redistribution occurs through a more spatially distributed diffusion network associated with its lower coordination number and larger characteristic transport distance.

The corresponding connectivity evolution is summarized in Fig. 3b. Before sealing, the interior void remains connected to the external surface and therefore does not constitute an enclosed cavity. Complete surface closure produces one or more enclosed cavity lobes, resulting in a discrete increase in the cavity-lobe count. The square and triangular lattices immediately form a single enclosed cavity that remains topologically unchanged throughout the subsequent evolution. In contrast, the honeycomb lattice initially forms two enclosed cavity lobes separated by the periodic support pillar. Continued surface diffusion enlarges the connecting neck between these lobes, producing a cavity-merging event that ultimately generates a single interconnected cavity.

Representative morphologies corresponding to these transitions are shown in Figs. 3c–f. Surface sealing isolates the buried cavity from the exterior void, whereas the cavity-merging event observed only in the honeycomb lattice establishes a single interconnected cavity through enlargement of the connecting neck. These observations demonstrate that post-sealing evolution is governed not only by continuous geometric smoothing but also by discrete topology transitions that determine the connectivity of the retained cavity. The resulting topology-dependent cavity architectures provide the structural basis for the transport analyses presented in the following sections.

3.3 Post-sealing structural relaxation

Following the topology transitions described above, the retained membrane–cavity structures continued to evolve through surface-diffusion-driven mass redistribution. The complete

temporal evolution of membrane thickness and cavity height is presented in Fig. S4. The square and triangular lattices rapidly approached nearly constant structural dimensions, whereas the honeycomb lattice exhibited substantially slower relaxation accompanied by larger spatial variations. This slower evolution reflects the more complex interconnected cavity geometry produced by the honeycomb topology.

The final membrane thicknesses and cavity heights are summarized in Fig. S5. Despite identical initial hole dimensions and nearest-neighbor spacing, the three lattice geometries produced distinctly different membrane–cavity structures. The square and triangular lattices yielded comparatively uniform membrane thicknesses and cavity heights, whereas the honeycomb lattice exhibited significantly larger spatial variations in both quantities. These differences reflect both the different initial void fractions and the non-axisymmetric interconnected cavity generated after the cavity-merging transition, which requires material redistribution over a broader spatial region during structural relaxation.

These observations demonstrate that lattice topology influences not only the final structural dimensions but also their spatial uniformity. The resulting differences in structural relaxation suggest that topology modifies the effective transport pathways available for long-range surface mass redistribution, motivating the transport-accessibility analysis presented in the following section.

3.4 Topology-dependent transport resistance and post-formation structural relaxation

Following cavity formation, the three lattice geometries exhibit different post-formation structural relaxation despite identical material properties, surface mobility, annealing conditions, and initial feature dimensions. For the square and triangular lattices, post-formation time begins immediately after surface sealing; for the honeycomb lattice, it begins after cavity merging produces a single interconnected retained cavity (Section S6). As summarized in Fig. 4, the triangular lattice relaxes most rapidly, whereas the honeycomb lattice exhibits substantially slower relaxation in both membrane thickness and cavity height. Because all simulations were performed under identical kinetic conditions, these differences cannot be explained solely by local surface curvature. Instead, they indicate that the global topology of the evolving Si/void interface regulates the accessibility of interconnected pathways available for long-range surface mass transport.

To quantify this effect, the extracted Si/void interface was represented as an undirected resistor network $G = (V, E)$, in which each diffuse-interface voxel corresponds to a graph node and neighboring vertices are connected by resistive edges. A unit potential difference was imposed between prescribed source and sink boundaries, and the network potential was obtained by solving the discrete Kirchhoff equation,

$$\sum_{j \in \mathcal{N}(i)} g_{ij}\left(V_i - V_j\right) = 0,$$

for every interior node, where g_{ij} denotes the conductance of the edge connecting neighboring nodes i and j. The resulting network-potential distributions are shown in Fig. 4a. Although identical boundary conditions were applied to all lattice geometries, the potential

fields differ substantially because the available transport pathways are determined by the evolving interface topology.

The effective network conductance was evaluated from the total current flowing through the resistor network, $G_{\mathrm{eff}} = I/\Delta V$, where I is the total current between the source and sink boundaries under the imposed potential difference ΔV. The normalized effective network conductance was defined as $G_{\mathrm{den}} = G_{\mathrm{eff}}/\overline{G}_{\mathrm{eff}}$, where $\overline{G}_{\mathrm{eff}}$ denotes the geometric mean of the effective conductances of the investigated lattice geometries. Accordingly, a normalized value of unity corresponds to the geometric-mean effective conductance across the three investigated lattice geometries, while values above and below unity indicate relatively higher and lower network conductance, respectively (Fig. 4b).

The normalized effective network conductance alone, however, does not fully explain the observed relaxation kinetics. Although the triangular lattice exhibits the highest network conductance, the square and honeycomb lattices have relatively similar conductance values despite their substantially different relaxation behavior. The honeycomb lattice also exhibits a considerably longer geodesic transport distance associated with its interconnected cavity geometry. These observations suggest that post-formation structural relaxation depends on both transport-path length and network accessibility rather than on network conductance alone.

To characterize the actual pathway followed by surface diffusion, we define the geodesic transport resistance as

$$R_{\mathrm{geo}} = \frac{L_{\mathrm{geo}}^4}{\phi_{\kappa}},$$

where L_{geo} is the effective geodesic transport distance along the evolving Si/void interface and ϕ_{κ} is the normalized curvature-driving descriptor. This expression follows from the characteristic scaling of surface-diffusion kinetics, for which the relaxation time scales with the fourth power of the transport distance and inversely with the curvature driving force [2,16]. Accordingly, R_{geo} represents the transport resistance expected when relaxation is governed solely by long-range diffusion along the interface.

Surface diffusion depends not only on the distance over which atoms migrate but also on the number and connectivity of the pathways available for mass transport. Even when two structures possess similar geodesic transport distances, a network containing multiple parallel pathways can redistribute mass more efficiently than one constrained to a limited number of routes. This behavior is analogous to current transport in an electrical resistor network [24], where additional parallel conducting paths increase the total current under the same potential difference. The effective network conductance therefore provides a physically meaningful measure of transport accessibility rather than merely geometric path length. This interpretation is conceptually related to resistance-based measures and graph Laplacian descriptions in graph theory [25,26], but the present formulation is adapted specifically to capillarity-driven surface diffusion and retains the classical L^4 scaling.

To incorporate transport distance and network accessibility simultaneously, we introduce the conductance-corrected transport resistance,

$$R_{\mathrm{CT}} = \frac{R_{\mathrm{geo}}}{G_{\mathrm{den}}} = \frac{L_{\mathrm{geo}}^4}{\phi_\kappa G_{\mathrm{den}}}.$$

Longer geodesic transport distances increase R_{CT}, whereas higher network conductance decreases it by enabling concurrent mass transport through multiple interconnected pathways. Thus, R_{CT} increases when either the diffusion pathway becomes longer or the accessibility of the interfacial transport network becomes poorer. Here, transport resistance is a relative descriptor rather than an electrical resistance or a directly measured material property; because the transport lengths enter to the fourth power, its numerical values depend on the length unit used in the calculation.

This formulation is physically motivated by the continuum description of capillarity-driven surface diffusion and the analogy with transport through interconnected resistor networks. Within the Mullins framework, the characteristic relaxation time depends inversely on the effective surface-transport coefficient [2,16]. The normalized effective network conductance provides a topology-dependent measure of transport accessibility, reflecting the connectivity of available interfacial pathways. Its inverse contribution to the conductance-corrected transport resistance is motivated by the enhanced transport capacity associated with multiple parallel pathways, rather than being treated solely as an empirical correction.

Figure 4c compares transport resistances based on Euclidean distance, geodesic distance, and the conductance-corrected formulation. Incorporating network accessibility yields a higher descriptive correlation with the characteristic relaxation times, as shown in Fig. 4d. The coefficient of determination increases from 0.723 to 0.853 for membrane-thickness relaxation and from 0.318 to 0.474 for cavity-height relaxation. The relatively weak correlation for cavity-height relaxation suggests that additional three-dimensional geometric constraints associated with cavity merging and interface reshaping contribute to its evolution. However, because each correlation is based on only three lattice geometries, these differences should be interpreted as preliminary trends rather than conclusive evidence of improved predictive capability. Moreover, the square and triangular lattices exhibit similar conductance-corrected transport resistances despite having different relaxation times, indicating that the proposed descriptor does not fully capture all factors governing structural relaxation. Nevertheless, the observed trends suggest that transport accessibility, together with diffusion distance, provides a physically meaningful descriptor for interpreting topology-dependent post-sealing relaxation. Further investigations involving additional lattice geometries are needed to establish its generality.

Figure 4e compares the normalized structural responses as a function of post-formation time before transport-resistance rescaling. Although all structural responses approach their respective steady states, with some transient overshoot beyond the normalized steady-state value, the relaxation rates differ substantially among the lattice geometries. The triangular lattice relaxes most rapidly, followed by the square lattice, whereas the honeycomb lattice exhibits the slowest evolution for both membrane thickness and cavity height. These pronounced differences indicate that a common time scale based solely on the elapsed post-formation time is insufficient to describe the relaxation behavior across different lattice topologies.

Motivated by these topology-dependent differences, the characteristic relaxation time is approximated by a linear relationship with the conductance-corrected transport resistance,

$$\tau = R_{\mathrm{CT}}C + b,$$

where C and b are the slope and intercept obtained from linear regression, respectively. Separate regression parameters are determined for membrane-thickness and cavity-height relaxation. Introducing the dimensionless conductance-corrected relaxation time,

$$\Theta_{\mathrm{CT}} = \frac{t - t_0}{R_{\mathrm{CT}}C + b},$$

where t_0 denotes the onset of retained-cavity relaxation for each lattice geometry, brings the structural responses of the three investigated lattice geometries into approximate collapse onto a common master curve (Fig. 4f). Both membrane-thickness and cavity-height evolutions are reasonably described by the first-order relaxation function,

$$1 - \exp(-\Theta_{\mathrm{CT}}).$$

Despite substantial differences in lattice topology and cavity morphology, the post-sealing structural responses of the three investigated lattice geometries exhibit broadly similar relaxation behavior when time is rescaled using the conductance-corrected transport resistance. This result suggests that both global transport distance and network accessibility contribute to the characteristic timescale of surface-diffusion-driven structural relaxation. The physical interpretation of this transport descriptor is further explored in the following section through direct visualization of the evolving surface-transport field. Because the rescaling parameters were obtained from the same three lattice geometries, the approximate collapse represents an internal consistency assessment rather than an independent validation of predictive capability. The first-order curve captures the overall relaxation timescale but not the transient overshoot observed in some responses.

3.5 Topology-dependent transport-field evolution

To independently evaluate the physical basis of the conductance-corrected transport resistance, the evolving surface-transport field was calculated directly from the phase-field simulation. The local surface transport flux is given by

$$\boldsymbol{J} = -M\nabla\mu,$$

where M is the surface mobility and μ is the chemical potential. Dense and spatially interconnected flux trajectories indicate efficient surface mass transport, whereas sparse or elongated trajectories indicate less efficient transport pathways.

Figures 5a–c show the logarithm of the in-plane flux magnitude, $\log_{10}|J_{xy}|$, evaluated on a common horizontal plane near the top membrane (z = 760 nm) immediately after complete surface closure. Because closure occurs at different dimensionless times for each lattice topology, the transport maps were extracted at the corresponding topology-specific closure times. Despite identical material properties and annealing conditions, markedly different transport fields emerge immediately after membrane formation. The square and triangular lattices develop relatively continuous annular pathways surrounding each sealed cavity, whereas the honeycomb lattice concentrates transport along the ligaments connecting neighboring cavities. Owing to its larger laterally connected cavity, the honeycomb lattice

distributes transport over a broader region while maintaining a lower overall flux intensity. These topology-dependent fields establish the initial transport conditions governing subsequent structural relaxation.

To quantify the overall transport process, the areal transport activity was defined as

$$A_J(t) = \frac{1}{A}\int_A w(\phi)\ \left|J_{xy}\right| dA,$$

where A denotes the horizontal cross-sectional area and $w(\phi) = 4\phi(1-\phi)$ is an interface-localization function that confines the integration to the diffuse Si/void interface. As shown in Fig. 5d, all three lattices exhibit initially high transport activity associated with rapid smoothing of the hole edges. The activity subsequently decreases as the local curvature is reduced during neck growth, surface closure, and post-sealing relaxation.

The magnitude and temporal evolution of A_J differ substantially among the lattice geometries. The triangular lattice maintains relatively high transport activity over much of the evolution, whereas the honeycomb lattice develops a weaker but more spatially distributed field after cavity merging. Although its transport pathways remain interconnected, mass redistribution in the honeycomb lattice proceeds along longer geodesic trajectories spanning the enlarged retained cavity. This longer transport distance, together with the relatively low network conductance, is consistent with the larger R_{CT} obtained in Section 3.4.

The cumulative transport was evaluated as

$$C_J(t) = \int_0^t A_J(t')\ dt'.$$

As shown in Fig. 5e, the triangular lattice accumulates the greatest total transport, followed closely by the square lattice, whereas the honeycomb lattice accumulates substantially less transport over the same dimensionless time interval. Figure 5f further shows that cumulative transport closely follows the normalized structural relaxation. Greater cumulative surface transport therefore corresponds directly to faster evolution of membrane thickness and cavity height.

The transport-field analysis provides complementary dynamic evidence supporting the resistor-network formulation. Whereas the network analysis quantifies the accessibility expected from the evolving interface topology, the flux field directly reveals how surface mass transport is spatially distributed and accumulated during morphological evolution. Their consistent trends support the interpretation that topology-dependent relaxation originates from the combined influence of transport-path length and network accessibility.

3.6 Physical implications of transport accessibility

The analyses in Sections 3.4 and 3.5 show that topology-dependent structural relaxation arises from two complementary transport factors. Local curvature provides the thermodynamic driving force, and the geodesic distance determines the characteristic migration length. Neither quantity, however, describes how efficiently material can be redistributed through the interconnected Si/void interface. This additional factor is captured by transport accessibility, which reflects the availability of parallel and connected surface-diffusion pathways.

The conductance-corrected transport resistance integrates these effects within a single physically motivated descriptor. The geodesic contribution preserves the characteristic fourth-power diffusion-length scaling, whereas the normalized effective network conductance represents the collective transport capacity of the evolving interface. Both quantities are extracted from the simulated morphology without fitting them to the observed relaxation times. The subsequent linear regression, however, introduces empirical coefficients that relate the conductance-corrected transport resistance to the characteristic relaxation time.

The results also support a broader interpretation of evolving interfaces as transport networks rather than solely geometric boundaries. Within this view, interface topology determines the organization and accessibility of the pathways through which long-range surface mass redistribution occurs. Morphologies with similar local curvature or Euclidean dimensions may therefore exhibit different relaxation kinetics when their interconnected transport pathways differ.

Although the present analysis is limited to three representative periodic hole lattices, the results highlight the influence of interface connectivity on surface mass redistribution and structural relaxation. From a practical perspective, lattice geometry may serve as a design parameter for controlling buried cavity morphology and membrane uniformity during silicon-on-nothing fabrication. In particular, the honeycomb lattice produces interconnected cavities and periodic support regions, suggesting a potential route toward supported membrane architectures, although their mechanical stability and performance remain to be evaluated. More broadly, the proposed transport analysis provides a physically motivated framework for interpreting topology-dependent structural evolution and may guide the design of diffusion-formed semiconductor structures.

4. Conclusion

In this study, we systematically investigated topology-dependent buried cavity formation in periodic hole lattices using three-dimensional phase-field simulations combined with topology-resolved transport analysis. By comparing square, triangular, and honeycomb lattices under identical material properties, geometric dimensions, and annealing conditions, the effects of lattice arrangement and evolving cavity connectivity were compared under matched feature dimensions and kinetic conditions, although initial void fractions differ among the lattices.

The results show that lattice topology influences post-sealing structural relaxation by regulating the accessibility of interconnected surface-diffusion pathways in addition to conventional geometric factors. Although local curvature provides the thermodynamic driving force and geodesic transport distance characterizes the migration length, neither quantity independently predicts relaxation kinetics. Instead, transport accessibility emerges as a key topology-dependent factor linking interface connectivity with long-range surface mass redistribution. Combining transport distance and accessibility in a conductance-corrected transport-resistance descriptor provides a physically motivated, preliminary framework for comparing structural relaxation across the three investigated lattice geometries.

The present findings highlight the importance of interface connectivity in surface-diffusion-driven morphological evolution. By combining phase-field simulations with graph-based transport analysis, this study provides a quantitative interpretation of how transport-path length and network accessibility contribute to the different relaxation behaviors of periodic silicon

membrane–cavity structures. These insights may support the design and optimization of diffusion-formed semiconductor architectures and motivate further investigations of transport accessibility in more complex interfacial geometries.

Acknowledgements
Not applicable.

Author contributions
JL: Writing, Editing. The author read and approved the final manuscript.

Funding
This work was supported by the Korea Evaluation Institute of Industrial Technology (KEIT) funded by the 2024 Materials and Components Technology Development Program (Ministry of Trade, Industry and Energy, Republic of Korea) (Project No. RS-2024-00443505) and the Technology Innovation Program (00144157, Development of Heterogeneous Multi-Sensor Micro-System Platform) funded by the Ministry of Trade, Industry & Energy (MOTIE, Korea).

Data availability
The simulation data and analysis outputs supporting the findings of this study are available from the corresponding author upon reasonable request.

Declarations
Competing interests
The author declares no competing interests. JL is the editor-in-chief of Micro and Nano Systems Letters. Editor-in-chief status has no bearing on editorial consideration.

References
1. Herring, J. E. Surface tension as a motivation for sintering. In *The Physics of Powder Metallurgy* (ed. Kingston, W. E.) 143–179 (McGraw-Hill, 1951).
2. Mullins, W. W. Theory of thermal grooving. *J. Appl. Phys.* **28**, 333–339 (1957).
3. Mizushima, I., Sato, T., Taniguchi, S. & Tsunashima, Y. Empty-space-in-silicon technique for fabricating a silicon-on-nothing structure. *Appl. Phys. Lett.* **77**, 3290–3292 (2000).
4. Thompson, C. V. Solid-state dewetting of thin films. *Annu. Rev. Mater. Res.* **42**, 399–434 (2012).
5. Sato, T., Aoki, N., Mizushima, I. & Tsunashima, Y. A new substrate engineering for the formation of empty space in silicon (ESS) induced by silicon surface migration. In *IEDM Technical Digest* 517–520 (1999).
6. Sato, T. et al. Fabrication of silicon-on-nothing structure by substrate engineering using the empty-space-in-silicon formation technique. *Jpn. J. Appl. Phys.* **43**, 12–18 (2004).
7. Hao, X. et al. Application of silicon-on-nothing structure for developing a novel capacitive absolute pressure sensor. *IEEE Sens. J.* **14**, 808–815 (2014).
8. Su, J. et al. Fabrication of a piezoresistive barometric pressure sensor by a silicon-on-nothing technology. *J. Sens.* **2019**, 5408268 (2019).
9. Wong, Y., Lorenzo, S., Miao, Y., Bregman, J. & Solgaard, O. Extended design space of silicon-on-nothing MEMS. *J. Microelectromech. Syst.* **28**, 850–858 (2019).
10. Lorenzo, S., Wong, Y. & Solgaard, O. Optical fiber-tip monolithic silicon pressure sensors. *IEEE Sens. J.* **20**, 2476–2484 (2020).
11. Kim, T., Ko, J. & Lee, J. Self-assembled silicon membrane resonator for high vacuum pressure sensing. *Vacuum* **201**, 111101 (2022).

12. Kim, J. et al. Hollow microtube resonators via silicon self-assembly toward subattogram mass sensing applications. *Nano Lett.* **16**, 1537–1545 (2016).
13. Sudoh, K., Iwasaki, H., Hiruta, R., Kuribayashi, H. & Shimizu, R. Void shape evolution and formation of silicon-on-nothing structures during hydrogen annealing of hole arrays on Si(001). *J. Appl. Phys.* **105**, 083536 (2009).
14. Sudoh, K., Hiruta, R. & Kuribayashi, H. Shape evolution of high aspect ratio holes on Si(001) during hydrogen annealing. *J. Appl. Phys.* **114**, 183512 (2013).
15. Depauw, V., Gordon, I., Beaucarne, G. & Poortmans, J. Large-area monocrystalline silicon thin films by annealing of macroporous arrays: understanding and tackling defects in the material. *J. Appl. Phys.* **106**, 033516 (2009).
16. Nichols, F. A. & Mullins, W. W. Morphological changes of a surface of revolution due to capillarity-induced surface diffusion. *J. Appl. Phys.* **36**, 1826–1835 (1965).
17. Cahn, J. W. & Hilliard, J. E. Free energy of a nonuniform system. I. Interfacial free energy. *J. Chem. Phys.* **28**, 258–267 (1958).
18. Chen, L.-Q. Phase-field models for microstructure evolution. *Annu. Rev. Mater. Res.* **32**, 113–140 (2002).
19. Provatas, N. & Elder, K. *Phase-Field Methods in Materials Science and Engineering* (Wiley-VCH, 2010).
20. Jeong, J., Kim, T., Lee, B. J. & Lee, J. Surrogate model for optimizing annealing duration of self-assembled membrane-cavity structures. *Micro Nano Syst. Lett.* **10**, 6 (2022).
21. Jeong, J., Kim, T. & Lee, J. Simulation of germanium-on-nothing cavity morphological transformation using deep learning. *Micro Nano Syst. Lett.* **10**, 22 (2022).
22. Dijkstra, E. W. A note on two problems in connexion with graphs. *Numer. Math.* **1**, 269–271 (1959).
23. Fiorio, C. & Gustedt, J. Two linear time union-find strategies for image processing. *Theor. Comput. Sci.* **154**, 165–181 (1996).
24. Doyle, P. G. & Snell, J. L. *Random Walks and Electric Networks* (Mathematical Association of America, 1984).
25. Klein, D. J. & Randić, M. Resistance distance. *J. Math. Chem.* **12**, 81–95 (1993).
26. Chung, F. R. K. *Spectral Graph Theory* (American Mathematical Society, 1997).

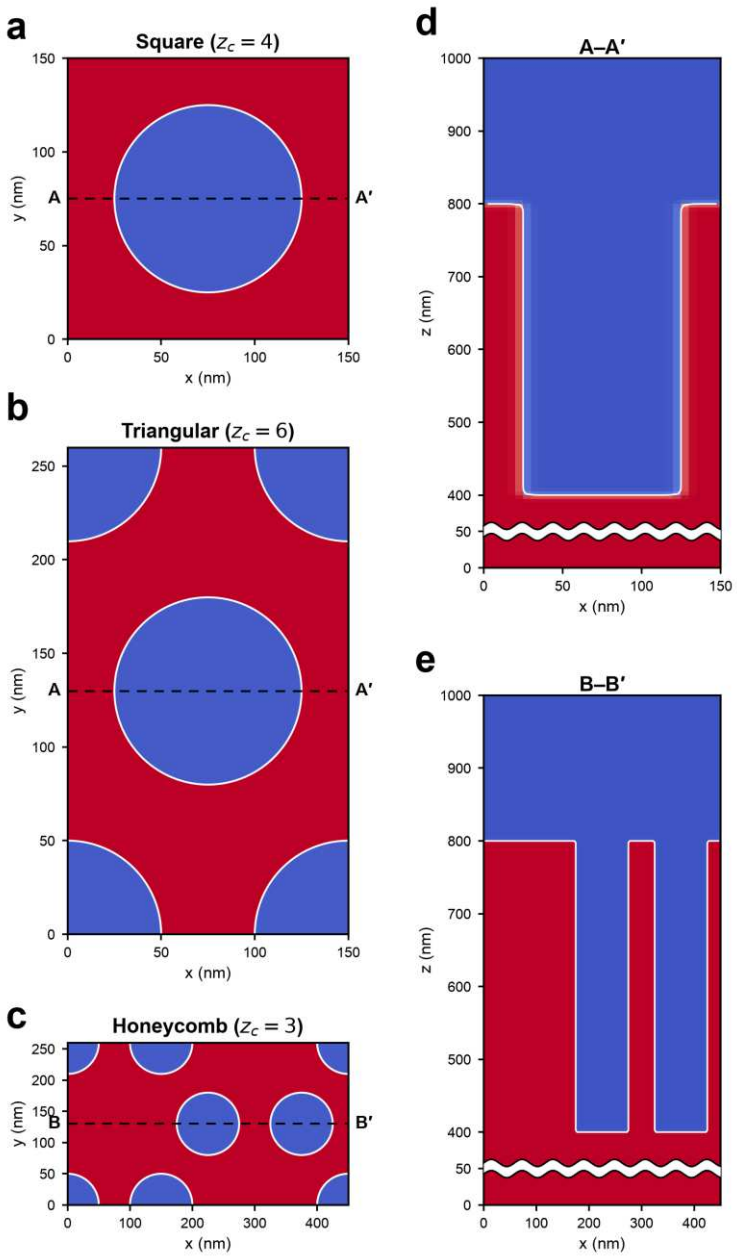


Figure 1 | Initial unit-cell geometries and corresponding cross-sectional configurations for three periodic hole lattices. (a) Top view of the square lattice (coordination number z_c = 4), showing the A–A′ cross-sectional plane. (b) Top view of the triangular lattice (z_c = 6) with the corresponding A–A′ cross-sectional plane. (c) Top view of the honeycomb lattice (z_c = 3), where the B–B′ section passes through the central support region between neighboring holes. (d) Initial X–Z cross section along A–A′ used for the square and triangular lattices. (e) Initial X–Z cross section along B–B′ for the honeycomb lattice. Periodic boundary conditions were applied in the lateral directions, while a zero-normal-flux boundary condition was imposed at the bottom surface. These geometries serve as the initial configurations for the phase-field simulations.

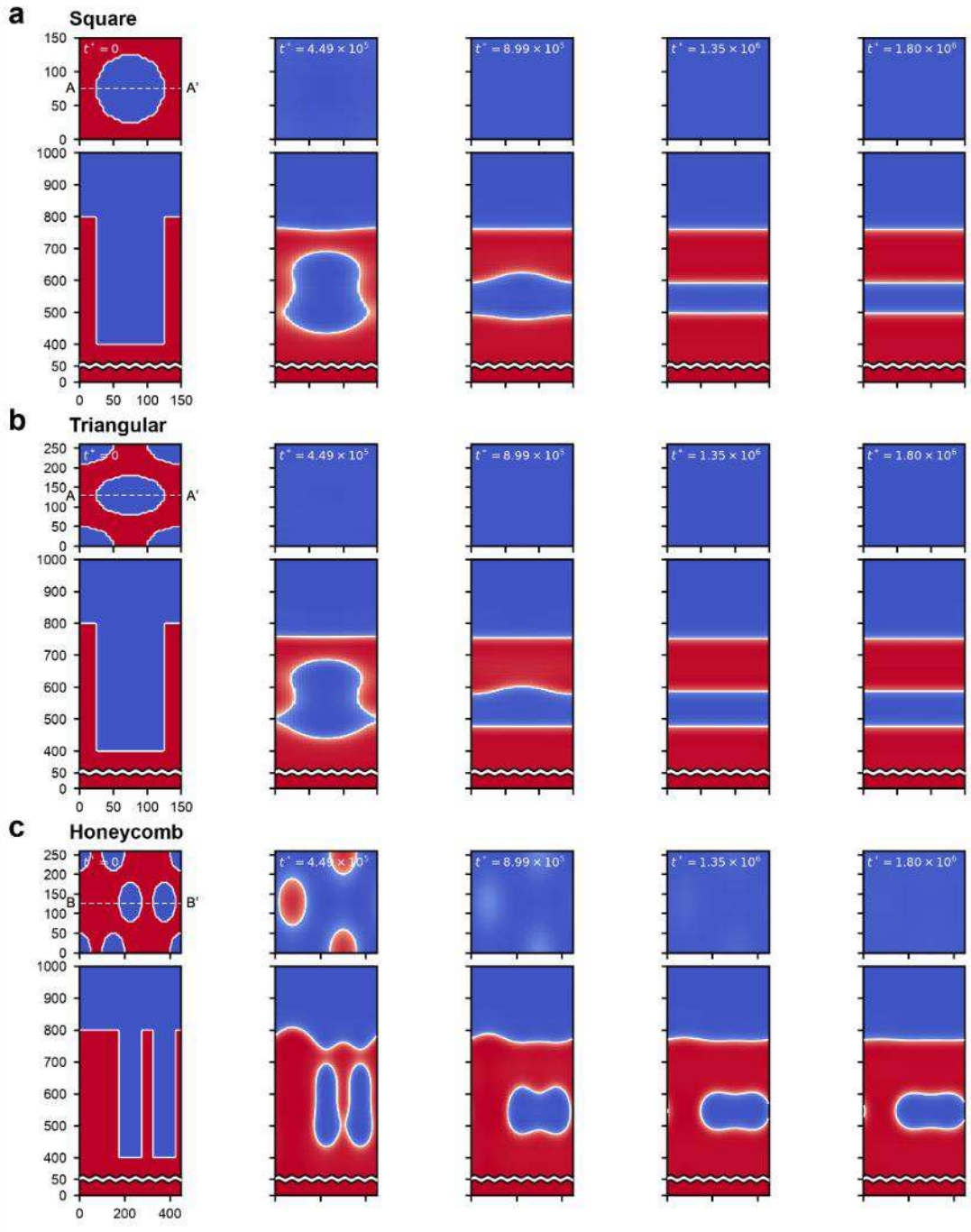


Figure 2 | Morphological evolution during surface-diffusion-driven buried cavity formation. Top-view (XY) phase-field profiles and the corresponding XZ cross sections extracted along the A–A′ (square and triangular lattices) and B–B′ (honeycomb lattice) lines are shown at selected dimensionless annealing times, t^*, for the (a) square, (b) triangular, and (c) honeycomb lattices. All simulations were performed using identical hole diameter, nearest-neighbor spacing, hole depth, film thickness, material properties, surface mobility, and annealing conditions. The omitted middle portion of each XZ panel is indicated by a broken axis for visualization. Although all three lattice geometries evolve toward membrane–cavity structures through surface-diffusion-driven sealing, they exhibit distinct sealing pathways, cavity morphologies, and post-sealing relaxation behaviors associated with differences in lattice topology. In the phase-field images, red indicates silicon and blue indicates void.

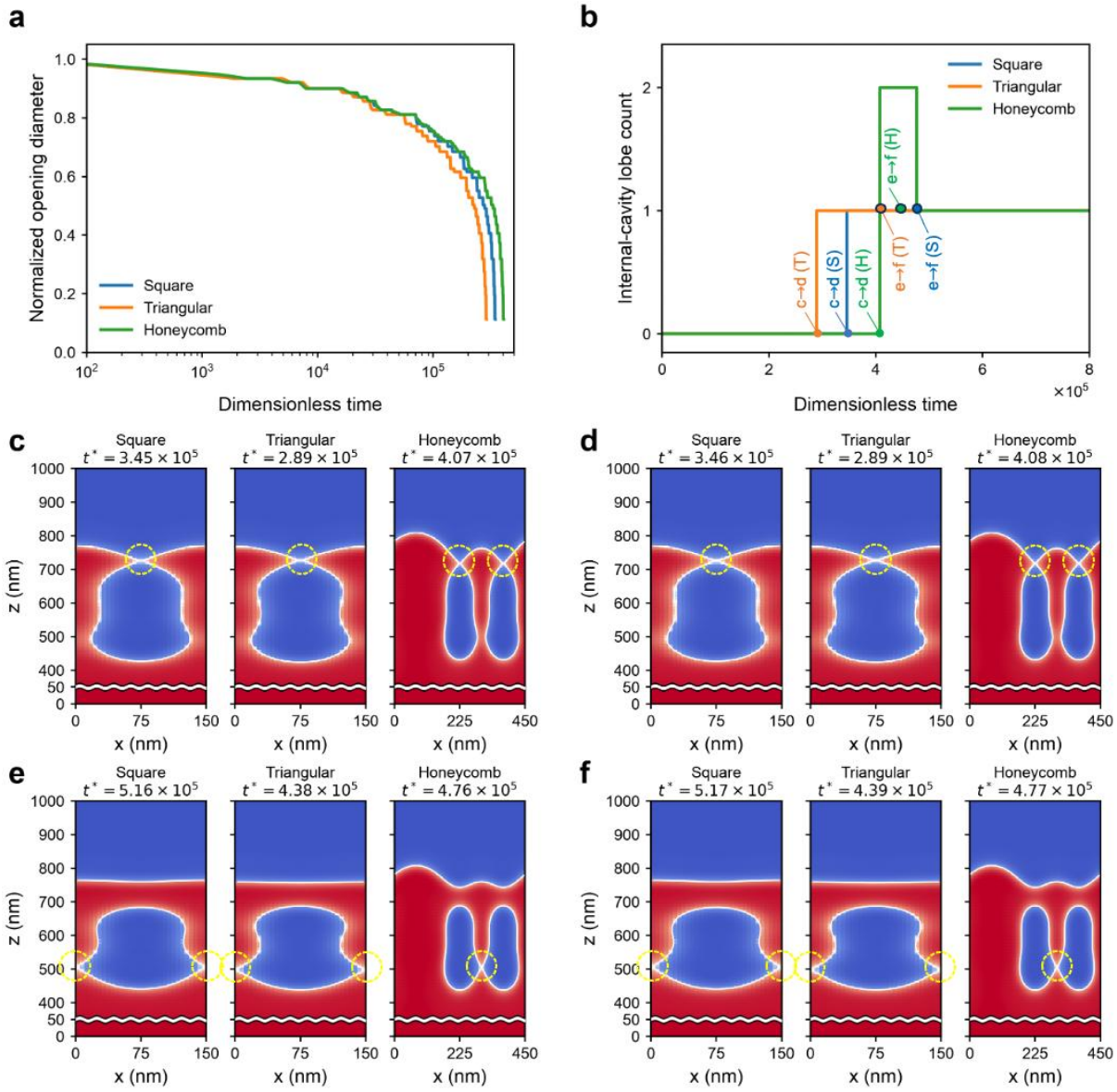


Figure 3 | Topological evolution during surface sealing and cavity formation. (a) Evolution of the normalized minimum surface-opening diameter as a function of dimensionless time, t^*, for the square, triangular, and honeycomb lattices. (b) Evolution of the number of connected internal-cavity lobes in the representative XZ section. The stepwise changes indicate topological transitions associated with the formation, merging, or splitting of enclosed cavity regions. (c, d) Representative XZ cross sections immediately before and after surface sealing, respectively. The dashed circles indicate the surface neck at which connectivity between the external void and the internal cavity is lost. (e, f) Representative XZ cross sections immediately before and after the subsequent cavity-topology transition, respectively. The dashed circles indicate the interfacial necks associated with changes in cavity connectivity. Topological events were identified by three-dimensional connected-component analysis under periodic lateral boundary conditions. Surface sealing was defined as the first loss of connectivity between the external surface-connected void and the retained internal cavity. In the phase-field cross sections, red indicates silicon and blue indicates void.

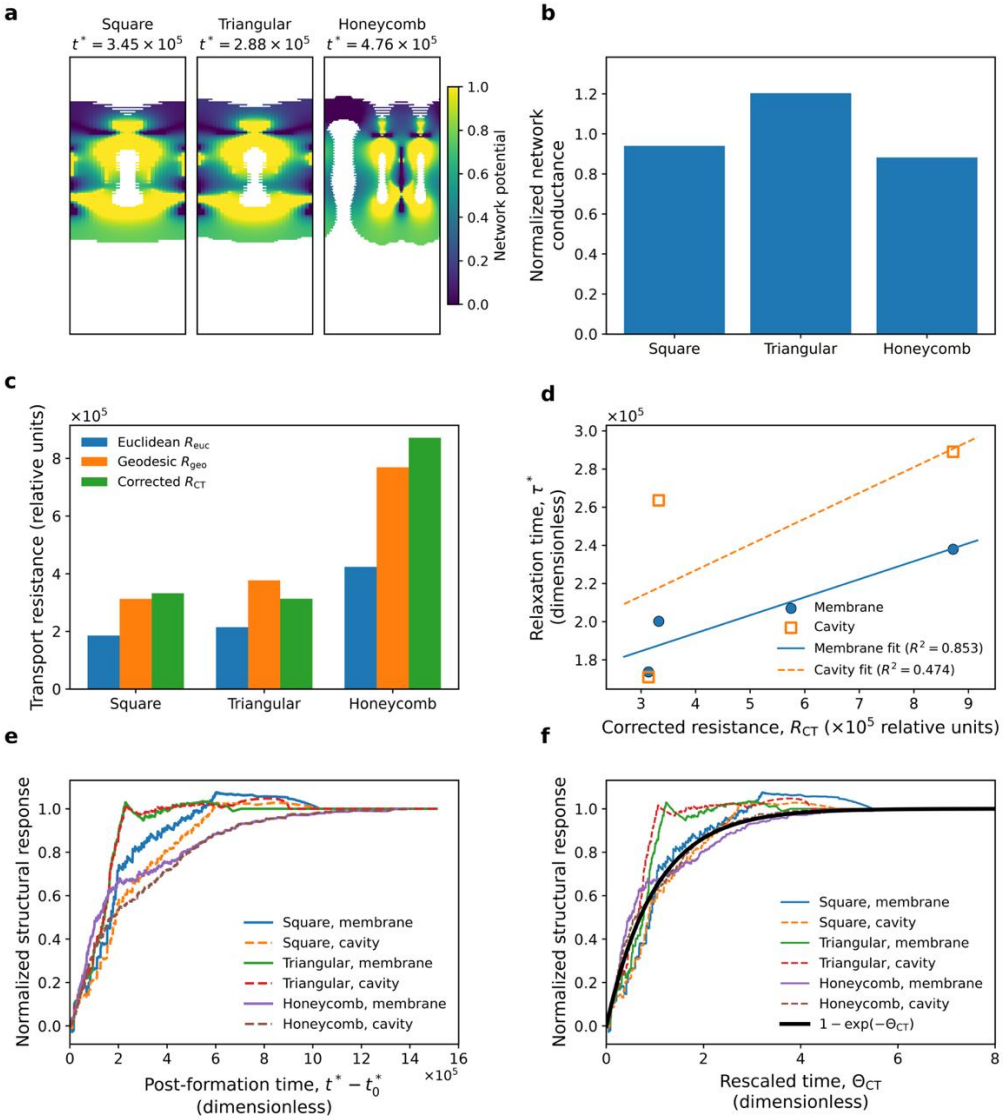


Figure 4 | Geodesic transport distance and network connectivity characterize post-formation structural relaxation. (a) Normalized network-potential distributions for representative square, triangular and honeycomb structures at the indicated dimensionless times, t^*. (b) Effective network conductance normalized by its geometric mean across the three lattices. (c) Comparison of Euclidean (R_{euc}), geodesic (R_{geo}) and conductance-corrected (R_{CT}) transport-resistance descriptors, reported in relative units. (d) Dimensionless relaxation times, τ^*, of membrane thickness and cavity height versus R_{CT}. Solid and dashed lines represent descriptive linear fits across the three lattices, rather than validated predictive relationships. (e) Normalized structural responses versus post-formation dimensionless time, $t^* - t_0^*$, with the time origin defined by surface sealing for the square and triangular lattices and cavity merging for the honeycomb lattice (Section S6). (f) Structural responses plotted against rescaled time, Θ_{CT}, defined as elapsed dimensionless time divided by the relaxation time estimated from the corresponding resistance–relaxation fit. The black line represents $1 - \exp(-\Theta_{CT})$. The approximate convergence of the responses suggests that transport-path length and network accessibility jointly influence post-formation relaxation kinetics. The resistance descriptors are relative quantities calculated using transport lengths in nanometres and are not dimensionless physical resistances. The first-order curve represents the overall trend and does not capture all transient overshoot.

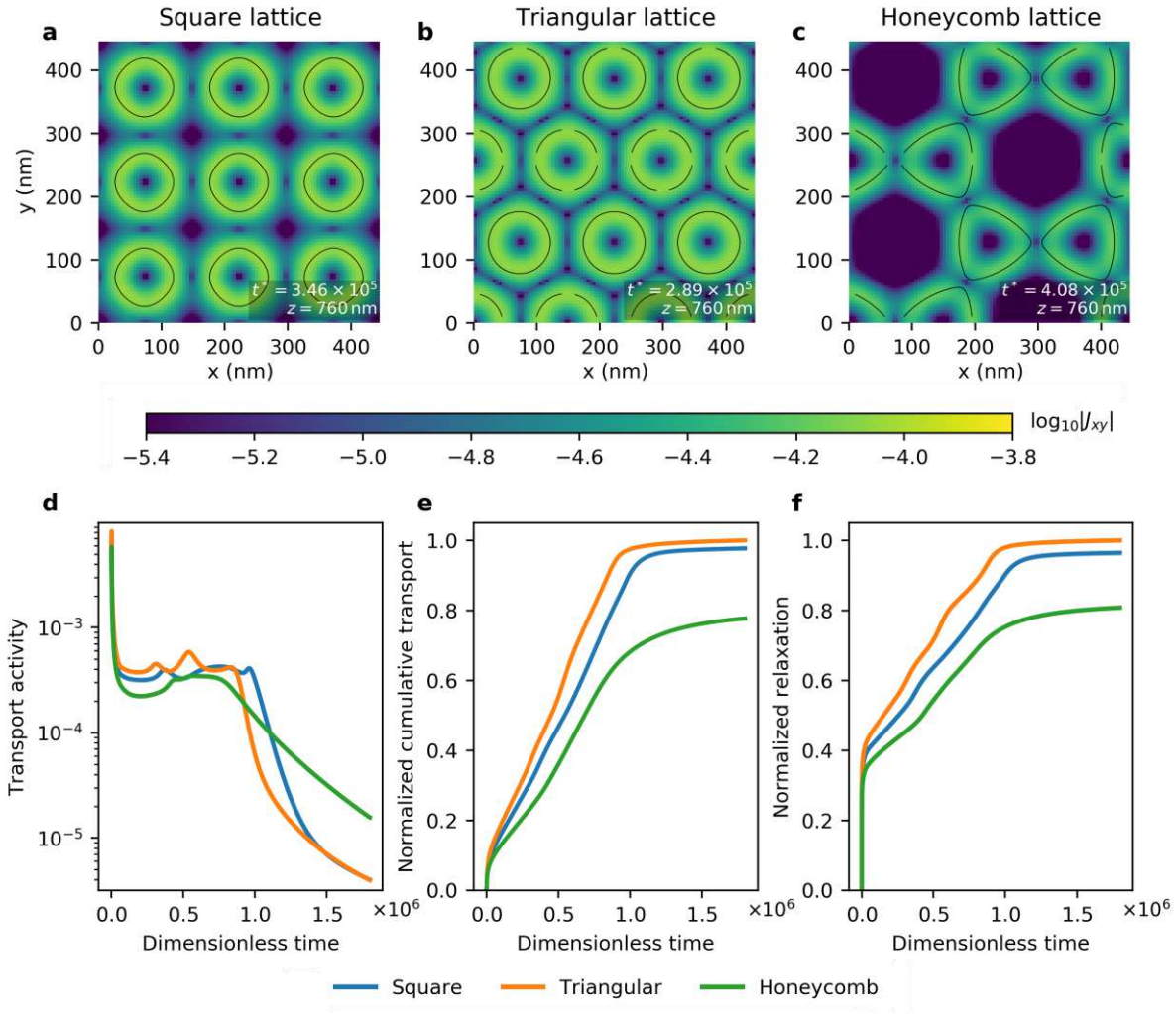


Figure 5 | Topology-dependent surface-transport fields and relaxation dynamics during buried cavity formation. (a–c) In-plane surface-transport flux magnitude evaluated on a common horizontal plane near the top membrane (z = 760 nm) immediately after complete surface closure for the square, triangular, and honeycomb lattices, respectively. Because surface closure occurs at different stages of evolution for each lattice topology, the transport maps were extracted at the corresponding topology-specific dimensionless times (t^*) indicated in each panel. A common logarithmic color scale was used to enable direct comparison of transport intensity among the lattice geometries. (d) Evolution of the areal transport activity during annealing, shown on a logarithmic scale as a function of dimensionless time, t^*. (e) Normalized cumulative transport referenced to the largest final cumulative transport among the three lattice geometries. (f) Normalized morphological relaxation referenced to the largest final morphology change among the three lattice geometries. The transport maps reveal distinct spatial distributions of surface-transport activity established immediately after membrane closure, while the transport activity, cumulative transport, and relaxation curves characterize the subsequent topology-dependent redistribution of surface mass. Together with Fig. 4, these results indicate that lattice topology influences transport accessibility and the associated kinetics of diffusion-driven structural relaxation.

Supplementary Files

This is a list of supplementary files associated with this preprint. Click to download.

- TopologydependentRevisedSupportingClean.docx